nature physics

Article

https://doi.org/10.1038/s41567-023-02216-y

Scaling behaviour and control of nuclear wrinkling

Received: 20 October 2022

Accepted: 21 August 2023

Jonathan A. Jackson [1,2,7], **Nicolas Romeo** [3,4,7], **Alexander Mietke** [3,5], **Keaton J. Burns** [3], **Jan F. Totz**[3], **Adam C. Martin** [1], **Jörn Dunkel** [3] ✉ & **Jasmin Imran Alsous** [6] ✉

The cell nucleus is enveloped by a complex membrane, whose wrinkling has been implicated in disease and cellular aging. The biophysical dynamics and spectral evolution of nuclear wrinkling during multicellular development remain poorly understood due to a lack of direct quantitative measurements. Here we characterize the onset and dynamics of nuclear wrinkling during egg development in the fruit fly when nurse cell nuclei increase in size and display stereotypical wrinkling behaviour. A spectral analysis of three-dimensional high-resolution live-imaging data from several hundred nuclei reveals a robust asymptotic power-law scaling of angular fluctuations consistent with renormalization and scaling predictions from a nonlinear elastic shell model. We further demonstrate that nuclear wrinkling can be reversed through osmotic shock and suppressed by microtubule disruption, providing tunable physical and biological control parameters for probing the mechanical properties of the nuclear envelope. Our findings advance the biophysical understanding of nuclear membrane fluctuations during early multicellular development.

Wrinkling and flickering of flexible sheet-like structures essentially determine the mechanics and transport in a wide range of physical and biological systems, from graphene[1,2] and DNA origami[3] to nuclear envelopes (NEs)[4–7] and cell membranes[8,9]. Over the last decade, much progress has been made through experimental and theoretical work in understanding the effects of environmental fluctuations on the bending behaviours of carbon-based monolayers[10] and the shape deformations of lipid bilayer membranes of vesicles[11–13] and cells[14,15]. In contrast, the emergence and dynamical evolution of surface deformations in NEs[6,7,16] at different length- and timescales, to which we refer throughout this paper simply as 'wrinkling', still pose fundamental open questions, as performing three-dimensional (3D) observations at high spatiotemporal resolution remains challenging under natural physiological and developmental growth conditions. Specifically, it is unclear how NE wrinkle formation proceeds during cellular development, which biophysical processes govern wrinkle morphology and whether there exist characteristic scaling laws for NE surface fluctuations[5,6,17]. Addressing these questions through quantitative measurements promises insights into the physics of complex membranes and can clarify the biological and biomedical implications of NE deformations that have been linked to gene expression[6], cellular aging[18] and diseases like progeria syndrome[4,19].

In this Article, we combine 3D confocal microscopy, theoretical analysis and simulations to characterize the wrinkling morphology and dynamics of nuclear surfaces in fruit fly egg chambers. A spectral analysis of over 300 nuclei provides evidence for an asymptotic power-law scaling of the surface fluctuations, consistent with predictions from renormalization calculations[20,21] and scaling arguments based on a nonlinear elasticity model for thin shells. Although the scaling is found to be highly robust against physical and biological perturbations,

---

[1]Department of Biology, Massachusetts Institute of Technology, Cambridge, MA, USA. [2]Graduate Program in Biophysics, Harvard University, Cambridge, MA, USA. [3]Department of Mathematics, Massachusetts Institute of Technology, Cambridge, MA, USA. [4]Department of Physics, Massachusetts Institute of Technology, Cambridge, MA, USA. [5]School of Mathematics, University of Bristol, Bristol, UK. [6]Center for Computational Biology, Flatiron Institute, Simons Foundation, New York, NY, USA. [7]These authors contributed equally: Jonathan A. Jackson, Nicolas Romeo. ✉e-mail: dunkel@mit.edu; jalsous@flatironinstitute.org

its magnitude (prefactor) can be tuned via osmotic pressure variation and microtubule disruption. These two different control mechanisms enable the tuning and probing of the NE's spectral and mechanical properties and provide biophysical strategies for suppressing and reversing nuclear wrinkling.

The NE is a double membrane that separates the cell's nuclear interior from the surrounding cytoplasm. The two concentric ~4-nm-thick lipid bilayers are ~20–50 nm apart and are supported by the nuclear lamina, a non-contractile meshwork of intermediate filaments that lie adjacent to the inner nuclear membrane, conferring mechanical stability and affecting essential cellular processes through the regulation of chromatin organization and gene expression[22,23]. Among other proteins, the NE contains nuclear pore complexes—multiprotein channels that primarily regulate the passage of macromolecules between the nucleus and the cytoplasm[24,25]. Recent in vitro studies have provided key insights into the role of lamins, cytoplasmic structures and the physical environment in affecting NE morphology, as well as evidence for the critical importance of nuclear shape for many cellular and nuclear functions[4,17], including transcriptional dynamics[6]. Despite notable progress, a quantitative understanding of how wrinkling phenomenology and 3D spectral properties of nuclear surfaces evolve in time and during cellular development has remained elusive.

To investigate the biophysical dynamics, scaling behaviours and reversibility of nuclear wrinkling, we used the egg chamber of the fruit fly *Drosophila melanogaster*, a powerful system amenable to 3D high-resolution live imaging and targeted biological and physical perturbations[26]. The egg chamber contains 15 nurse cells and the oocyte (the immature egg cell), all connected via cytoplasmic bridges and enclosed by a thin layer of hundreds of follicle cells (Fig. 1a; Supplementary Fig. 1 shows the schematic[27]). For most of the ~3 days of oogenesis, the nurse cells supply proteins, mRNAs and organelles to the oocyte through diffusion and microtubule-mediated directed transport[28–31]. To provide the prodigious amount of material and nutrients that the oocyte needs, each nurse cell replicates its DNA ~10 times without undergoing cell division, thereby considerably increasing its nuclear and cell sizes[32]. In the ~30 h window studied here, the diameter of the nurse cell nuclei in the cells directly connected to the oocyte increases from approximately 16 to about 40 µm (refs. 32,33), accompanied by the progressive appearance of fold-like deformations in the NE, providing an ideal test bed for studying the onset and evolution of NE wrinkling (Fig. 1b,c).

To compare nurse cell nuclei within the same egg chamber and across different egg chambers, we defined a proxy measurement for developmental time (referred to here as the 'time proxy') based on the geometric average of the egg chamber's length and width (Methods, Supplementary Section III-1 and Supplementary Fig. 1b,c). Since the egg chamber geometry closely correlates with developmental progression, adopting this continuous geometric characterization offers finer temporal resolution than the traditional approach of distinguishing 14 discrete morphological stages[28,29] (Supplementary Fig. 1c provides a comparison between the time proxy and developmental stage). By time ordering nuclei according to this metric, we could more accurately determine the time of emergence of nuclear wrinkling and reconstruct its evolution (Fig. 1b,c). To track the NEs of nurse cells in space and time, we used a fluorescently tagged version of the nuclear pore complex protein Nup107 that delineates the nucleus (Supplementary Video 1; Supplementary Fig. 2 shows the qualitatively similar wrinkling patterns using a different labelled protein in the NE and via label-free imaging). Note that this label allows the observation of only deformations that include both membranes of the NE but is unlikely to label deformations that include only the inner membrane, such as type-I nucleoplasmic reticula[34,35]. Having acquired highly resolved 3D imaging data (Fig. 1c and Supplementary Fig. 3), we reconstructed the nuclear surface radius $R(\theta,\phi)$ relative to the geometric centre of the nucleus, where θ and ϕ are the spherical polar angles.

To obtain a compact 3D spectral representation of the nuclear surface deformations, we computed the real spherical harmonic coefficients f_{lm}, defined by

$$R(\theta,\phi)=\sum_{l=0}^{l_{\max}}\sum_{m=-l}^{l} f_{lm}Y_{lm}(\theta,\phi), \tag{1}$$

where Y_{lm} is the spherical harmonic with angular number l and order m (Methods). Equation (1) allows for a continuous reconstruction of the NEs (Fig. 1d and Supplementary Fig. 3), with the mode-cutoff $l_{\max}$ setting the angular resolution of the spectral representation (Methods). The coefficient values $\{f_{lm}\}$ depend on the choice of coordinate system, that is, the orientation of the nuclei. To obtain a rotation-invariant characterization of the surface wrinkles, we consider the power spectrum of radial out-of-plane deformations as

$$P_l=\frac{4\pi}{(2l+1)f_{00}^2}\sum_{m=-l}^{l} f_{lm}^2, \tag{2}$$

normalized by the average radius of the shell $\langle R\rangle = f_{00}/\sqrt{4\pi}$. The non-negative numbers P_l measure the average power in a mode of angular wavenumber l. A single-valued summary statistic of surface wrinkling can be given in terms of the 'roughness' parameter $\mathrm{Ro}=\sum_{l\geq 3}(2l+1)P_l$, the total power contained in angular numbers $l \geq 3$. By ignoring the long-wavelength modes $l < 3$, Ro measures the contribution of finer-scale wrinkles to NE deformations. Our analysis of over 300 nurse cell nuclei shows that the power spectrum of NEs maintains an approximately constant shape as development progresses, but with a steadily increasing amplitude (Fig. 1e and Supplementary Fig. 4), reflecting the fact that wrinkling becomes more pronounced as the nuclei increase in size. Ro increases exponentially with the time proxy (Fig. 1f), suggesting that nurse cell nuclei smoothly transition from an unwrinkled to a wrinkled state.

Nuclear surface wrinkling is a highly dynamic process[6]. By imaging individual nurse cells at ~40 s intervals, we too observed that the NE surface shapes substantially fluctuate, with smaller features appearing and disappearing faster than larger ones (Fig. 1g and Supplementary Video 2). Specifically, power spectra P_l of repeatedly imaged nuclei changed on timescales of minutes or faster (Supplementary Figs. 4 and 5). The rotational invariance of the spectra implies that these fluctuations are not the result of whole-body rotations, but instead reflect a rapid shape dynamics of NE surfaces. Experimental limitations prevented the quantification of timescales for the entire 3D surface, but our observations are qualitatively consistent with findings that smaller wrinkles typically decay faster[15,36]. Furthermore, the fact that the deformation spectrum is monotonically decreasing (Fig. 1e) implies that there is no preferred wavelength, suggesting that the observed NE shapes do not correspond to fluctuations about the steady states of buckled shells, but instead reflect dynamic wrinkling across all the experimentally resolved angular scales.

Both maximum-intensity projections (MIPs) and spectral reconstructions show that NE wrinkles and creases are sharp, with narrow bent regions separated by flatter areas (Fig. 1). This morphology is reminiscent of the nonlinear stress-focusing characteristic of crumpled elastic sheets and shells such as ordinary paper sheets, which are much more easily bent than stretched[1,37,38]. In particular, these geometric nonlinearities lead to anisotropic responses when point forces are applied to the shell[38]. To rationalize the experimentally observed wrinkle morphology at spatial scales larger than the NE thickness, we constructed a minimal effective elastic model, describing the NE as a deformed spherical shell (equilibrium radius R). In spherical coordinates $\mathbf{r}=(\theta,\phi)$, the shell has an isotropic elastic free energy of[21,39]

$$F_{\mathrm{shell}}=\int \mathrm{d}^2\mathbf{r}\left[\frac{\kappa}{2}\left(\nabla^2 f\right)^2+\frac{\lambda}{2}\epsilon_{ii}^2+\mu\epsilon_{ij}^2\right], \tag{3}$$

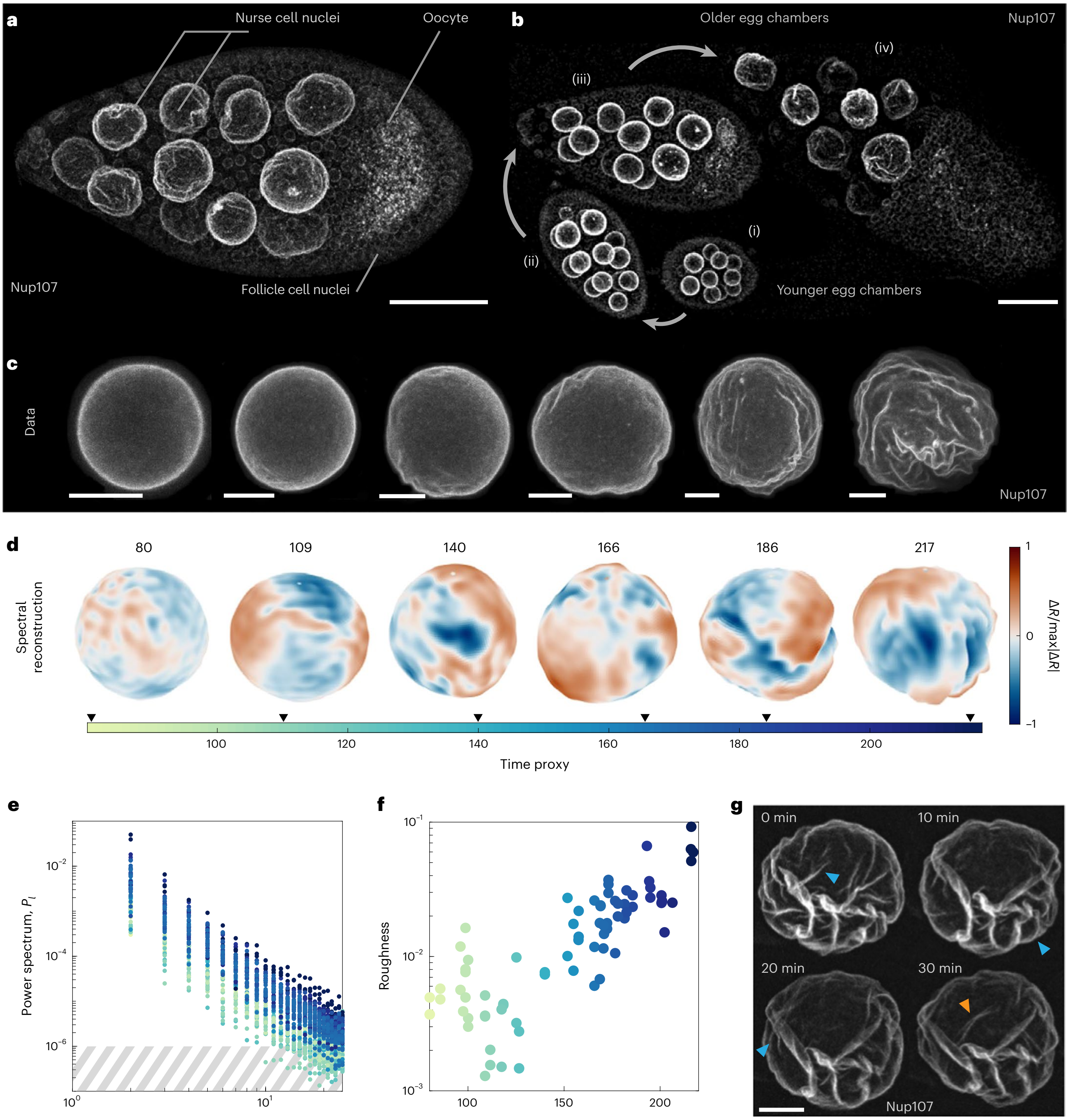

Fig. 1 | Dynamic wrinkling of nurse cell's NEs during *Drosophila* egg development. a, MIP of a 3D image of an egg chamber expressing GFP-labelled Nup107, a component of the nuclear pore complex. The wrinkled nuclei of the 15 nurse cells are substantially larger than those of the surrounding follicle cells. **b**, MIP of four egg chambers showing an increase in nurse cell nuclear size and nuclear surface deformation as the egg chambers age. The curved arrows indicate developmental progression from the youngest (i) to the oldest (iv). **c**, MIPs of individual nurse cell nuclei from six egg chambers spanning all of the ages included in our dataset, showing an increase in nuclear radius and NE wrinkling with age. Note that the scale bar is the same size for each image; the oldest nucleus shown is about 2.3 times the diameter of the youngest shown. **d**, Spectral reconstruction of NE surfaces shown in **c** from the 3D microscopy data using spherical harmonics with an angular number up to $l_{\max} = 25$ (equation (1) and Methods). Time proxy values for each nucleus are included above the reconstructions. **e**, Power spectra normalized by the average radius for $N = 78$ nuclei from 39 egg chambers in nurse cells directly connected to the oocyte (results are qualitatively similar for nuclei farther away from the oocyte; Supplementary Fig. 4). The hashed area indicates the approximate noise threshold for young nuclei; the colour indicates the time proxy (corresponding to the colour bar in **d**) as defined in the main text and detailed in Supplementary Section III-1. **f**, NE roughness Ro $= \sum_{l\geq 3}(2l+1)P_l$ for the same nuclei as in **e** increases exponentially with time proxy (Supplementary Fig. 4). **g**, Snapshots of the same nucleus at four different time points illustrate that NE wrinkling is a dynamic process (Supplementary Video 2). The blue and orange arrowheads point to wrinkles that disappear and appear, respectively, between subsequent frames. Scale bars, 50 µm (**a** and **b**); 10 µm (**c** and **g**).

where $i,j \in \{\theta, \phi\}$ and using the Einstein summation convention. The energy functional (equation (3)) accounts for bending stiffness through a Helfrich-like bending term that penalizes out-of-plane deformation f (positive when pointing inwards) and the stretching of the membrane through the nonlinear strain tensor ϵ_{ij}. The two-dimensional Lamé parameters λ and μ are proportional to two-dimensional Young's modulus Y. The strain combines contributions from f and from the in-plane deformation $\mathbf{u}(\mathbf{r})$ (Supplementary Section IV). We also allow for a preferred radius of curvature R_c of the shell mismatched with radius R of the shell $R_c \geq R$, which in the large-Föppl–von Kármán (FvK) regime leads to a strain tensor $\epsilon_{ij} = \frac{1}{2}\left(\partial_i u_j + \partial_j u_i + \partial_i f \partial_j f\right) - \delta_{ij} f/R_c$ (Supplementary Section IV). Previous work[40–42] has shown the NE to be stiffer than most biological membranes and to be well described as a thin membrane of a 3D isotropic elastic material with an effective 3D Young's modulus of $E \approx 1$ kPa and thickness of $h \approx 10$–100 nm (Supplementary Section IV-5 provides a more detailed discussion of the limitations of fluid membrane models), leading to a bending rigidity of $\kappa = 100$–$300 kT_{\mathrm{eq}} \approx 10^{-18}$ J (T_{eq} is the room temperature) and a stretching rigidity captured by the two-dimensional Young modulus of $Y \approx 10^{-4}$ N m^{-1} (ref. 43). By construction, these moduli are approximately related through the effective thickness $h \approx \sqrt{\kappa/Y}$ (ref. 21). Note that Y is a factor of 10^3 smaller than the stretching rigidity of a lipid bilayer, potentially explained by the presence of 'area reservoirs' in NEs and by conformational changes in transmembrane proteins[44]. For a shell of radius R, one can define the FvK number $\gamma = YR^2/\kappa$, which describes the relative propensity of the material to bend rather than to stretch. Using the above values, we find that the NE has a large FvK number of $\gamma \approx 10^4$–10^6, comparable with that of a sheet of paper or graphene[1]. Accordingly, the NE is more amenable to bend than to stretch, and deformations are expected to appear as sharp wrinkles and creases, in agreement with our observations (Fig. 1).

To compare the surface shapes and fluctuation predicted by equation (3) with our experimental data, we simulated the equilibrium Langevin partial differential equation derived from this free energy (Methods and Supplementary Section IV-4 provide the simulation details). The simulations account for hydrodynamic coupling and both passive and active fluctuations, which are modelled by an effective temperature kT_{eff}. Despite the model's minimal character and theoretical limitations of equation (3) at long wavelengths where $l \to 0$ (Supplementary Section IV), the numerically obtained shapes (Fig. 2a) are qualitatively similar to those in the experiments (Fig. 1d). In the experimentally accessible range of low-to-intermediate angular wave numbers ($3 \lesssim l \lesssim 11$), the angular spectra extracted from the simulations at different ratios of $kT_{\mathrm{eff}}/\kappa \in [0.05, 0.50]$ (Fig. 2b) and experimental data (Fig. 1e) also show an approximately similar decay, suggesting that the minimal elastic shell model in equation (3) captures relevant features of the NE, providing a basis for further analysis and predictions.

The main feature of the experimentally measured spectra is that both younger and older nuclei exhibit a similar asymptotic power-law decay in the limit of small angular numbers $l \leq 10$ (Fig. 2c). To rationalize this observation, we first note that the scaling behaviour in our experiments deviates from the basic linear response theory predictions, which is expected because even for younger nuclei, the radial fluctuations f typically exceed the NE thickness $h \approx 10^{-3}R$ (Fig. 1c–f). More precisely, for small fluctuations ($f \ll h \ll R$) and small thermodynamic pressures ($p \ll p_c = 4\sqrt{\kappa Y}/R_c^2$, where p_c is the critical buckling pressure of the sphere), linear response theory predicts that the power spectrum P_l exhibits a plateau for $l \leq l_c$ and falls off as l^{-4} for $l \gg l_c$ with a crossover value of $l_c \approx \gamma^{1/4}\sqrt{R/R_c}$ (Supplementary Section IV)[21,45], which is not seen in our experiments (Figs. 1e and 2c). Indeed, classical shell theory[2] states that nonlinear effects become important when the out-of-plane deformations f become comparable with or exceed the shell thickness h, which is generally the case in our data where $h \ll f \ll R$ (Fig. 1c,d,g). Nonlinear analysis of elastic plates and shells has a long history[20,46] and has seen major advances in the last decade[21,39], motivated in part by the discovery of graphene[47]. As demonstrated above, the FvK number of the NE is comparable with that of graphene, so we can borrow and apply recent theoretical results to understand the fluctuation spectra of the NE. Specifically, a detailed renormalization group (RG) analysis[21,48] of equation (3) showed that for sufficiently small plate fluctuations, elastic nonlinearities lead to a modified asymptotic decay of $P_l \propto l^{-3.2}$, consistent with our experimental and simulated data (Figs. 1e and 2b,c) and with previous experiments in red blood cell spectrin networks[49]. In particular, earlier studies[20,21,39] also predicted that the interplay of elastic nonlinearities and fluctuations can cause the spontaneous collapse of sufficiently large shells, suggesting a physical mechanism that could contribute to the eventual breakdown of the nurse cell's NE when these cells donate their contents to the oocyte[30,50].

The previously mentioned RG methods can give rise to divergences in large deformation regimes, where nonlinearities dominate the shell's response (Supplementary Section IV and Supplementary Fig. 9). To obtain an analytical prediction for the scaling in the larger-deformation regime $h \ll f \ll R < R_c$, relevant to older nuclei, we performed an asymptotic dimensional analysis that provides additional insights into how NE wrinkling can be controlled. To that end, we added an effective pressure term $F_{\mathrm{p}} = -\int \mathrm{d}^2\mathbf{r}\, p_{\mathrm{eff}} f$ to the elastic free energy F_{shell}, where p_{eff} accounts for a normal load, which may arise from osmotic pressure differences or microtubule-induced local stresses. Using L to denote the length scale of the characteristic surface variation and omitting numerical prefactors that depend on details of the adopted thin-shell modelling approach (Supplementary Section IV), one finds that for shells of thickness $h \approx \sqrt{\kappa/Y}$, the various free energy components give scaling contributions of the form[21]

$$\frac{\delta F}{Y} \approx \left(\frac{h}{L}\right)^2 \left(\frac{f}{L}\right)^2 + \left(\frac{f}{R_c}\right)^2 + \frac{f}{R_c}\left(\frac{f}{L}\right)^2 + \left(\frac{f}{L}\right)^4 - \frac{p_{\mathrm{eff}} f}{Y}. \tag{4}$$

The first term corresponds to bending and the second and third terms arise from the non-zero curvature of the undeformed shell. The fourth term describes the nonlinear response associated with changes in the Gaussian curvature of the shells. For well-developed wrinkles with $f \gg h$, the first term can be neglected as it is smaller than the fourth term. Considering wrinkle amplitudes f_l at the spatial length scale of $L \approx R/l$, where l is the angular wavenumber, the remaining terms can be recast as

$$\frac{\delta F_l}{Y} \approx \left(\frac{f_l}{R_c}\right)^2 + \frac{f_l}{R_c}\left(\frac{f_l}{R}\right)^2 l^2 + \left(\frac{f_l}{R}\right)^4 l^4 - \frac{p_{\mathrm{eff}}}{Y} f_l. \tag{5}$$

Since $R_c > R$, the first two terms will be dominated by the l^4 term, implying that at the steady state, this quartic term and the pressure term must balance out, consistent with a corresponding earlier result for flat plates with $R_c = \infty$ (ref. 2). We, thus, find $f_l \approx (p_{\mathrm{eff}}/Y)^{1/3}(R/l)^{4/3}$, and hence, for the angular power spectrum $P_l \approx (f_l/R)^2$ (equation (2)), the scaling law becomes

$$P_l \approx \left(\frac{p_{\mathrm{eff}} R}{Y}\right)^{2/3} l^{-8/3}. \tag{6}$$

In this scaling regime, the surface deformation dynamics is dominated by the shell's resistance to stretching, which causes changes in its Gaussian curvature[51]. Both our experimental data (Fig. 2c and Supplementary Fig. 4) and spherical shell simulations (Supplementary Fig. 8) show an asymptotic spectral decay $P_l \propto l^{-\alpha}$ with an exponent α in the range of $8/3 < \alpha < 3.2$, predicted by the scaling analysis and RG calculations.

Both equation (6) and the robustness of the experimentally observed scaling behaviour in time (Fig. 2c and Supplementary Fig. 4) and under different chemical and physical perturbations (Fig. 3) suggest that the emergence of NE wrinkling is primarily controlled by the material properties and the effective pressure p_{eff} induced by thermal and active fluctuations. For Gaussian fluctuations with

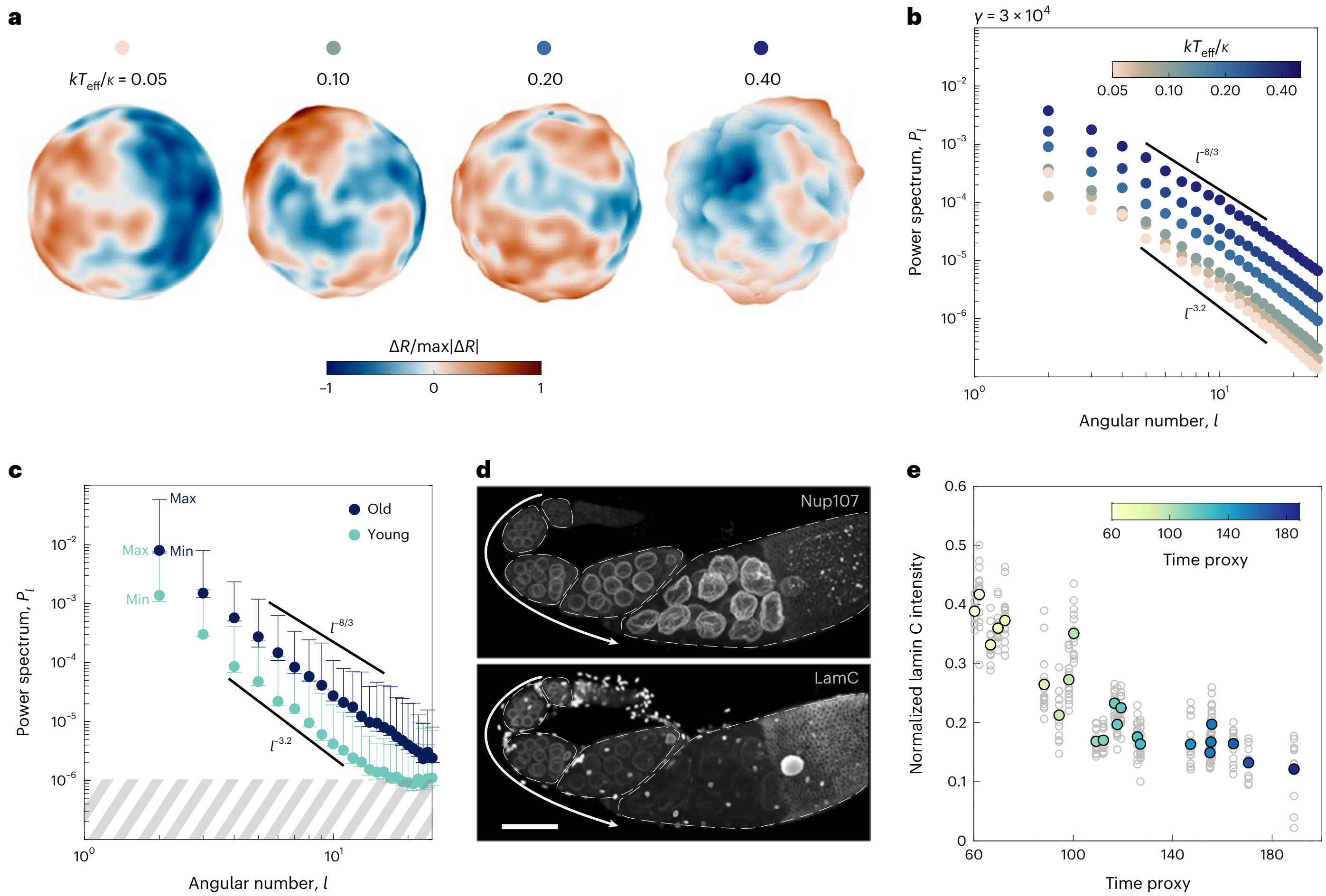

Fig. 2 | Fluctuating elastic shell theory predicts a scaling law with exponent of ~3 for the wrinkle power spectrum, in agreement with experiments. **a**, Equilibrium simulation snapshots of nuclei at temperature $T_{\rm eff} = 10T_{\rm eq}$, undeformed radius $R = 25$ μm and $R_c/R = 20$, at a fixed FvK number of $\gamma = 3 \times 10^4$ for varying elastic moduli controlled by $kT_{\rm eff}/\kappa$. The colour indicates the normalized deviation of the surface from the mean shell radius. **b**, Time-averaged spectra of the simulated NEs of undeformed radius $R = 25$ μm, $R_c/R = 20$ and $T_{\rm eff} = 10T_{\rm eq}$ for different moduli κ and Y at fixed $\gamma = 3 \times 10^4$, showing the transition from weak nonlinearity to strong nonlinearity as the bending rigidity decreases. The colour bar matches the dots from **a**. **c**, Binned averages of spectra from nuclei in nurse cells directly connected to the oocyte reveal that shape fluctuations follow a scaling law with an exponent between −3.2 and −8/3 that is obeyed throughout development. 'Young' nuclei have a time proxy between 80 and 140, $N = 29$ nuclei, 12 egg chambers; 'old' nuclei have a time proxy between 160 and 220, $N = 40$ nuclei, 22 egg chambers. The bars show extremal values. The hashed area indicates the approximate noise threshold for young nuclei. (Supplementary Figure 4 shows a comparison between the nuclei at different positions in the egg chamber). **d**, Fixed egg chambers expressing Nup107::RFP and stained for lamin C, showing a decrease in lamin C intensity in nurse cell nuclei as the egg chambers increase in age. In contrast, the Nup107::RFP intensity stays relatively constant. The same trend is observed in the live imaging of egg chambers expressing LamC::GFP and Nup107::RFP (Supplementary Fig. 6a). The wrinkling of nuclei in younger egg chambers (all but the rightmost) results from fixation and is not observed in live imaging until later stages. The arrows indicate increasing age; the egg chamber boundaries are shown by the dashed outlines. Scale bar, 50 μm. **e**, Normalized lamin C fluorescence intensity decreases approximately fivefold over time. Methods provides the normalization details. $N = 337$ nuclei from 23 egg chambers; the coloured dots show the means for each egg chamber.

effective temperature $T_{\rm eff}$, previous theoretical work[21,39] showed that $p_{\rm eff} \approx p_c(kT_{\rm eff})\sqrt{\gamma} \approx (Y/R)(kT_{\rm eff}/\kappa)$, where $p_c = 4\sqrt{\kappa Y}/R^2$ is the critical buckling pressure for a homogeneous spherical shell. If in addition to a fluctuating pressure p', there are uniform loads, such as those caused by osmotic pressure differences, we find $p_{\rm eff} = p'(R/\langle R\rangle)^3$ accounts for excess area contributions to the amplitude (as long as the shell is not stretched taut; Supplementary Section IV-3). Inserting these results into equation (6), the scaling analysis predicts that wrinkle formation can be tuned by changing the bending rigidity κ, the activity $kT_{\rm eff}$ and the cell's osmotic pressure balance (Supplementary Section IV-2.4 provides a comparison with RG predictions).

To test these predictions and investigate the role of the NE's material structure during wrinkle formation, we performed live-imaging experiments in which we measured the concentration of a structural component that determines nuclear stiffness. Elastic properties of the NE are known to strongly depend on the nuclear lamina[52], a roughly 10–100-nm-thick meshwork of intermediate filaments that abuts the NE's inner membrane[22]. *Drosophila* have two lamin proteins, namely, lamin C (a developmentally regulated A-type lamin similar to mammalian lamin A/C[53,54]) and lamin Dm0 (a B-type lamin present in most cell types). Through the live imaging of egg chambers simultaneously expressing a fluorescently labelled nuclear pore complex protein (Nup107) and lamin C as well as through fixed imaging with an antibody against lamin C, we found that as the egg chambers age and the nurse cells grow in size, the ratio of lamin C to Nup107 decreases (Fig. 2d,e and Supplementary Fig. 6a–c), whereas the intensity of Nup107 remains roughly constant (Supplementary Fig. 6d). Nonetheless, at the experimentally resolved spatial scales, lamin C continues to appear alongside Nup107 at the sites of wrinkles (Supplementary Fig. 6e–i). This reduction in lamin C concentration might cause

https://doi.org/10.1038/s41567-023-02216-y

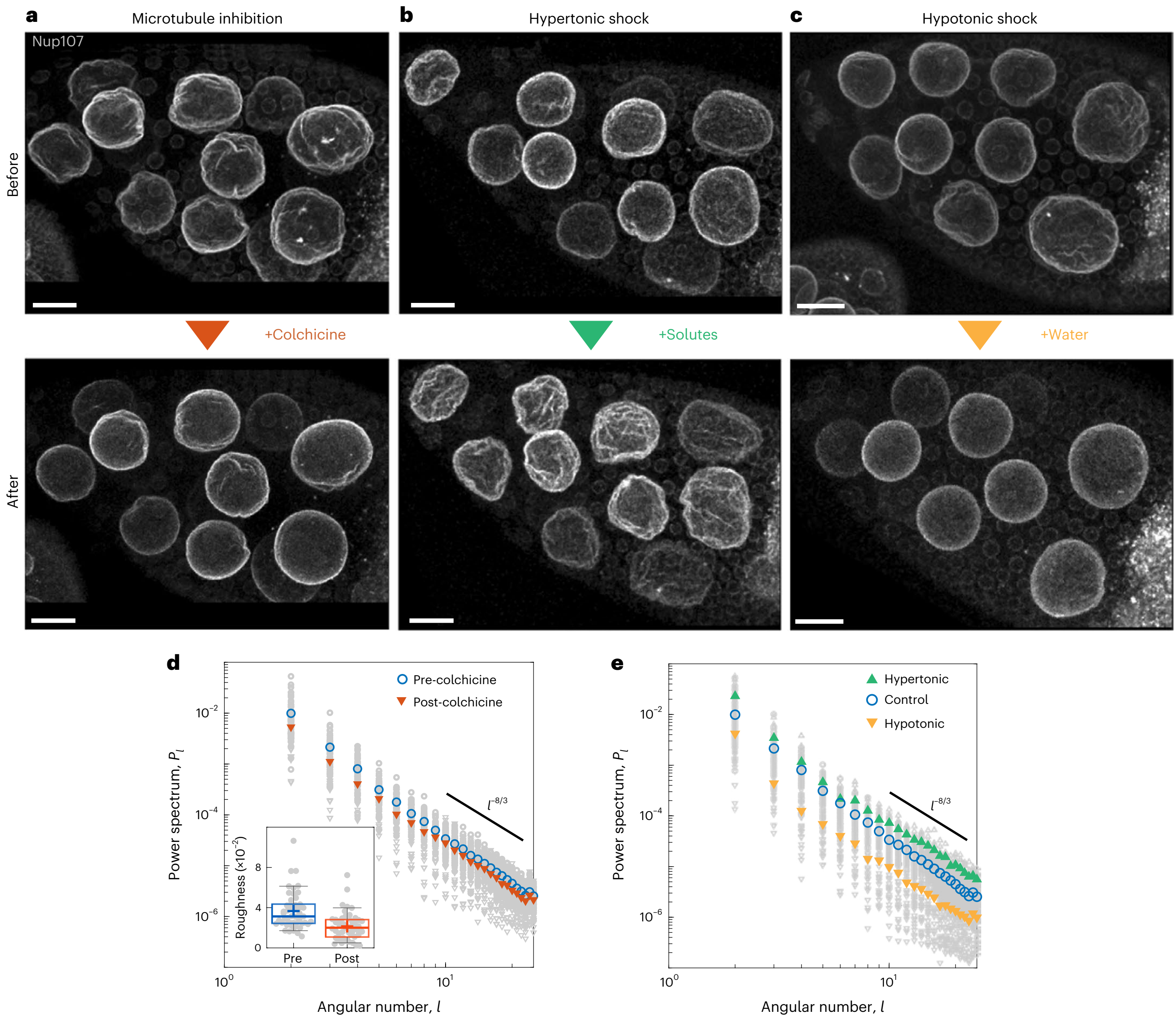

Fig. 3 | Perturbation experiments confirm the robustness of observed scaling laws and reveal NE wrinkling reversal mechanisms. a, MIP of one egg chamber before (top) and after (bottom) the inhibition of microtubule polymerization by colchicine, showing that microtubule disruption can reverse wrinkling (Supplementary Video 4). **b**, MIPs before and after hypertonic shock using an external culture medium of 1.5× osmolarity, showing an increase in wrinkling. **c**, MIPs before and after hypotonic shock using an external culture medium of 0.5× osmolarity, showing a decrease in wrinkling. Egg chambers in **a**–**c** have time proxies of 171, 174 and 171, respectively. **d**, Power spectrum after microtubule inhibition by colchicine still follows a power law with roughly the same exponent, with a reduction in roughness by a factor of 2 (inset). $N = 49$ pre-colchicine and post-colchicine nuclei, from six egg chambers for time proxies 169–182. For box plots, the plus signs denote mean; middle line is the median; the top and bottom edges of the box are the upper and lower quartiles, respectively; and whiskers span from 9% to 91% of the data range. **e**, In the presence of increased inwards (hypertonic) or outwards (hypotonic) pressure, the overall shape of the power spectrum remains approximately conserved. Hypotonic shock treatment reduces the wrinkle amplitudes, providing a reversal mechanism for NE wrinkling. The spectra were computed using 49 control, 15 hypertonic and 30 hypotonic nuclei in the time proxy range 165–185, from 6, 3 and 6 egg chambers, respectively, using nuclei from all the nurse cells rather than only those directly connected to the oocyte. Supplementary Figure 7 shows the roughness values over a larger range of time proxies. Scale bar, 20 µm.

the softening of NE and a reduced bending rigidity κ that increases wrinkle amplitudes[52], as predicted by equation (6). However, given the challenge in performing perturbative studies (Supplementary Section I-6), it is not possible to assess the functional importance of lamin C decrease from our data.

In addition to material properties, active fluctuations[55] or hydrodynamic effects[11,56] can substantially affect buckling and pattern formation in shells and membranes[12,57,58]. To explore how changes in cytoskeleton-mediated intracellular activity[59] influence the spectrum of NE deformation, we performed additional perturbation experiments targeting the cytoplasmic microtubule and actin networks. Previous work showed that incoherent microtubule dynamics can cause fluctuations in NE during cellularization of the *Drosophila* embryo[60]. Consistent with this earlier report and with the predictions of equation (6), we found that the inhibition of microtubule polymerization by the small-molecule inhibitor colchicine considerably reduces the amplitude of fluctuations (Fig. 3a, Supplementary Fig. 11a,b and Supplementary Videos 4 and 5). Colchicine treatment also decreased the nucleus volume by 5–20%; however, as a volume decrease for a similar surface area would lead to a rougher rather than smoother NE in the absence of other factors, it is unlikely that volume reduction explains the effects seen on colchicine treatment. Furthermore, colchicine addition reduced the motion of cytoplasmic contents of the cells (Supplementary Videos 6 and 7), suggesting that microtubule-mediated active fluctuations contribute to NE wrinkling. However, colchicine addition in older egg chambers (time proxies roughly over 185) had a less noticeable effect, decreasing the rotational motion of nuclei but not leading to the same extent of observable unwrinkling as in younger egg chambers. In contrast, the perturbation of actin by cytochalasin D did not unwrinkle the NE (Supplementary Fig. 11c,d and Supplementary Videos 8 and 9), suggesting that cytoplasmic F-actin is not a major contributor to NE wrinkling during the developmental stages studied here. The observation that the inhibition of microtubule polymerization reduces the wrinkle amplitude but does not change the spectral scaling behaviour (Fig. 3d) suggests that to the leading order, non-equilibrium contributions to NE fluctuations arising from microtubule dynamics can be modelled through an effective temperature kT_{eff} (refs. 9,15). We also tested other mechanisms known to contribute to NE deformation, such as sustained impingement by cytoskeletal filaments or changes to chromatin structure (Supplementary Section II), but found lamin C decrease to be the dominant factor correlating with NE wrinkle formation (Supplementary Figs. 10, 11 and 12 and Supplementary Video 3). Nonetheless, other factors than the ones addressed in this study could also participate in NE wrinkling, as our model is a simplification of a complex biological process.

Equation (6) also suggests that osmotic pressure variations can—by tuning the available excess area[61,62]—enhance or reverse wrinkle formation by up- or downshifting the deformation spectrum without changing its characteristic decay. To test this prediction, we performed osmotic shock experiments and found that adding salt to the ambient culture medium (hypertonic shock) increases the total external pressure on the NE, which drives fluid out of the nucleus and leads to visibly more wrinkled surfaces (Fig. 3b,e). Conversely, reducing the salt concentration in the culture medium (hypotonic shock) decreases the external pressure and leads to the substantial smoothening of wrinkled NE (Fig. 3c,e and Supplementary Fig. 7; Supplementary Section I-5 provides the experimental details and Supplementary Section IV-3 provides an explanation of the connection between osmotic pressure and wrinkle amplitude). In both cases, NEs maintained their altered morphology for 15–30 min before nuclear shapes trended back towards their pre-shock state, presumably through regulatory mechanisms that partially compensate for osmotic changes. In agreement with equation (6), the spectral slopes remained approximately preserved for both types of shock. Taken together, these results support the hypothesis that wrinkle morphology and the dynamics of deformation of the nurse cells' NE are dominated by a nonlinear elastic response rather than liquid-like behaviour.

NE wrinkles have been associated with biological processes including nuclear positioning[6], and as a mechanosensitive element of the cell, the NE can regulate chromatin dynamics and force-induced transcription factor movement through nuclear pore complexes[16,63–65]. Here, we observed an increase in NE wrinkling during egg chamber growth that correlates with an increase in nuclear size along with a decay in lamin C concentrations. Although NE wrinkling may affect the nurse cells' chromatin organization and transcriptional states, NE wrinkles may instead simply result from concomitant nucleus growth and decrease in lamin C density in cells that are fated to die to enable egg development. It is nonetheless tempting to propose that NE wrinkles could act as a tension buffer: tension applied to the NE would initially unfold the wrinkles before leading to substantial in-plane strain that might cause NE rupture. Such a two-stage response to tension has indeed been observed during cell spreading, in which an NE stretch-mediated response occurs only after the initially wrinkled nucleus flattens by a certain amount[5,17].

Prior work has shown that some nurse cells in stages 5–9 egg chambers have a high level of intranuclear actin, which decreases from stage 10 onwards[66]. Additionally, in other contexts such as the *Drosophila* larval muscle, lamin C mutants can induce the formation of intranuclear actin rods and potentially deform the nuclei[67]. These findings suggest that changes in intranuclear actin levels or organization may also affect wrinkling; however, whether they increase or decrease wrinkling remains unclear (Supplementary Section II). Another future prospect is to investigate how NE wrinkling changes when the lamin C density is exogenously modified, allowing further comparisons with theory and clarifying whether NE wrinkling has a biological function. Due to complications with existing fly reagents for perturbing lamin C levels in the female germline, increasing or decreasing the expression of lamin C in the nurse cell's NEs proved challenging (Supplementary Section I-6); therefore, developing such genetic tools would constitute a substantial technical advance. A further limitation of our study is that the continuum model is a simplification of the complex anatomy of the NE and that our measurements cannot distinguish between features that only include a single NE membrane layer or are below the resolution limit of confocal light microscopy.

To conclude, our experimental and theoretical results suggest that the essential qualitative aspects of NE wrinkling can be understood within the framework of nonlinear elastic thin-shell mechanics. As NEs have an FvK number similar to both graphene and paper[1], we expect our theoretical observations to be relevant for these and other similar systems, where fluctuations push the membranes and shells into larger-deformation regimes. With the power-law exponent set by the elastic behaviour of the shell, the amplitude of wrinkles is controlled by the effective pressure, which we have manipulated here through osmotic shocks and microtubule inhibition. Our findings, therefore, raise the question of whether cellular control over pressure could be a generic biophysical mechanism for avoiding undesirable consequences of NE wrinkling[4,17,19].

Online content

Any methods, additional references, Nature Portfolio reporting summaries, source data, extended data, supplementary information, acknowledgements, peer review information; details of author contributions and competing interests; and statements of data and code availability are available at https://doi.org/10.1038/s41567-023-02216-y.

References

1. Blees, M. K. et al. Graphene kirigami. *Nature* **524**, 204–207 (2015).
2. Los, J. H., Fasolino, A. & Katsnelson, M. I. Mechanics of thermally fluctuating membranes. *npj 2D Mater. Appl.* **1**, 9 (2017).
3. Yoo, J. & Aksimentiev, A. In situ structure and dynamics of DNA origami determined through molecular dynamics simulations. *Proc. Natl Acad. Sci. USA* **110**, 20099–20104 (2013).
4. Kalukula, Y., Stephens, A. D., Lammerding, J. & Gabriele, S. Mechanics and functional consequences of nuclear deformations. *Nat. Rev. Mol. Cell Biol.* **23**, 583–602 (2022).
5. Lomakin, A. J. et al. The nucleus acts as a ruler tailoring cell responses to spatial constraints. *Science* **370**, eaba2894 (2020).
6. Almonacid, M. et al. Active fluctuations of the nuclear envelope shape the transcriptional dynamics in oocytes. *Dev. Cell* **51**, 145–157.e10 (2019).
7. Biedzinski, S. et al. Microtubules control nuclear shape and gene expression during early stages of hematopoietic differentiation. *EMBO J.* **39**, e103957 (2020).
8. Brochard, F. & Lennon, J. F. Frequency spectrum of the flicker phenomenon in erythrocytes. *J. Phys.* **36**, 1035–1047 (1975).

9. Betz, T., Lenz, M., Joanny, J.-F. & Sykes, C. ATP-dependent mechanics of red blood cells. *Proc. Natl Acad. Sci. USA* **106**, 15320–15325 (2009).
10. Bowick, M. J., Košmrlj, A., Nelson, D. R. & Sknepnek, R. Non-Hookean statistical mechanics of clamped graphene ribbons. *Phys. Rev. B* **95**, 104109 (2017).
11. Kantsler, V., Segre, E. & Steinberg, V. Vesicle dynamics in time-dependent elongation flow: wrinkling instability. *Phys. Rev. Lett.* **99**, 178102 (2007).
12. Kokot, G., Faizi, H. A., Pradillo, G. E., Snezhko, A. & Vlahovska, P. M. Spontaneous self-propulsion and nonequilibrium shape fluctuations of a droplet enclosing active particles. *Commun. Phys.* **5**, 91 (2022).
13. Honerkamp-Smith, A. R., Woodhouse, F. G., Kantsler, V. & Goldstein, R. E. Membrane viscosity determined from shear-driven flow in giant vesicles. *Phys. Rev. Lett.* **111**, 038103 (2013).
14. Ben-Isaac, E. et al. Effective temperature of red-blood-cell membrane fluctuations. *Phys. Rev. Lett.* **106**, 238103 (2011).
15. Turlier, H. et al. Equilibrium physics breakdown reveals the active nature of red blood cell flickering. *Nat. Phys.* **12**, 513–519 (2016).
16. Chu, F.-Y., Haley, S. C. & Zidovska, A. On the origin of shape fluctuations of the cell nucleus. *Proc. Natl Acad. Sci. USA* **114**, 10338–10343 (2017).
17. Venturini, V. et al. The nucleus measures shape changes for cellular proprioception to control dynamic cell behavior. *Science* **370**, eaba2644 (2020).
18. Scaffidi, P. & Misteli, T. Lamin A-dependent nuclear defects in human aging. *Science* **312**, 1059–1063 (2006).
19. Mounkes, L. C., Kozlov, S., Hernandez, L., Sullivan, T. & Stewart, C. L. A progeroid syndrome in mice is caused by defects in A-type lamins. *Nature* **423**, 298–301 (2003).
20. Nelson, D., Piran, T. & Weinberg, S. *Statistical Mechanics of Membranes and Surfaces—Proceedings of the 5th Jerusalem Winter School for Theoretical Physics* (World Scientific, 1989).
21. Košmrlj, A. & Nelson, D. R. Statistical mechanics of thin spherical shells. *Phys. Rev. X* **7**, 011002 (2017).
22. Aebi, U., Cohn, J., Buhle, L. & Gerace, L. The nuclear lamina is a meshwork of intermediate-type filaments. *Nature* **323**, 560–564 (1986).
23. Lammerding, J. et al. Lamin A/C deficiency causes defective nuclear mechanics and mechanotransduction. *J. Clin. Investig.* **113**, 370–378 (2004).
24. Strambio-De-Castillia, C., Niepel, M. & Rout, M. P. The nuclear pore complex: bridging nuclear transport and gene regulation. *Nat. Rev. Mol. Cell Biol.* **11**, 490–501 (2010).
25. Knockenhauer, K. E. & Schwartz, T. U. The nuclear pore complex as a flexible and dynamic gate. *Cell* **164**, 1162–1171 (2016).
26. Hudson, A. M. & Cooley, L. Methods for studying oogenesis. *Methods* **68**, 207–217 (2014).
27. King, R. C., Rubinson, A. C. & Smith, R. F. Oogenesis in adult *Drosophila melanogaster*. *Growth* **20**, 121–157 (1956).
28. McLaughlin, J. M. & Bratu, D. P. *Drosophila melanogaster* oogenesis: an overview. in *Drosophila Oogenesis, Methods in Molecular Biology* Vol. 1328 (eds Bratu, D. P. & McNeil, G. P.) 1–20 (Springer, 2015).
29. Bastock, R. & St Johnston, D. *Drosophila* oogenesis. *Curr. Biol.* **18**, R1082–R1087 (2008).
30. Imran Alsous, J. et al. Dynamics of hydraulic and contractile wave-mediated fluid transport during *Drosophila* oogenesis. *Proc. Natl Acad. Sci. USA* **118**, e2019749118 (2021).
31. Mahajan-Miklos, S. & Cooley, L. Intercellular cytoplasm transport during *Drosophila* oogenesis. *Dev. Biol.* **165**, 336–351 (1994).
32. Lin, H. & Spradling, A. C. Germline stem cell division and egg chamber development in transplanted *Drosophila germaria*. *Dev. Biol.* **159**, 140–152 (1993).
33. Tzur, A., Kafri, R., LeBleu, V. S., Lahav, G. & Kirschner, M. W. Cell growth and size homeostasis in proliferating animal cells. *Science* **325**, 167–171 (2009).
34. Malhas, A. N. & Vaux, D. J. *Nuclear Envelope Invaginations and Cancer* 523–535 (Springer, 2014).
35. Fricker, M., Hollinshead, M., White, N. & Vaux, D. Interphase nuclei of many mammalian cell types contain deep, dynamic, tubular membrane-bound invaginations of the nuclear envelope. *J. Cell Biol.* **136**, 531–544 (1997).
36. Zilman, A. G. & Granek, R. Undulations and dynamic structure factor of membranes. *Phys. Rev. Lett.* **77**, 4788–4791 (1996).
37. Andrejevic, J., Lee, L. M., Rubinstein, S. M. & Rycroft, C. H. A model for the fragmentation kinetics of crumpled thin sheets. *Nat. Commun.* **12**, 1470 (2021).
38. Witten, T. A. Stress focusing in elastic sheets. *Rev. Mod. Phys.* **79**, 643–675 (2007).
39. Paulose, J., Vliegenthart, G. A., Gompper, G. & Nelson, D. R. Fluctuating shells under pressure. *Proc. Natl Acad. Sci. USA* **109**, 19551–19556 (2012).
40. Guilak, F., Tedrow, J. R. & Burgkart, R. Viscoelastic properties of the cell nucleus. *Biochem. Biophys. Res. Commun.* **269**, 781–786 (2000).
41. Funkhouser, C. M. et al. Mechanical model of blebbing in nuclear lamin meshworks. *Proc. Natl Acad. Sci. USA* **110**, 3248–3253 (2013).
42. Kim, D.-H. et al. Volume regulation and shape bifurcation in the cell nucleus. *J. Cell Sci.* **128**, 3375–3385 (2015).
43. Dahl, K. N., Kahn, S. M., Wilson, K. L. & Discher, D. E. The nuclear envelope lamina network has elasticity and a compressibility limit suggestive of a molecular shock absorber. *J. Cell Sci.* **117**, 4779–4786 (2004).
44. Enyedi, B. & Niethammer, P. Nuclear membrane stretch and its role in mechanotransduction. *Nucleus* **8**, 156–161 (2017).
45. Pécréaux, J., Döbereiner, H.-G., Prost, J., Joanny, J.-F. & Bassereau, P. Refined contour analysis of giant unilamellar vesicles. *Eur. Phys. J. E* **13**, 277–290 (2004).
46. Landau, L. D. & Lifshitz, E. M. *Theory of Elasticity. Number 7 in Course of Theoretical Physics* (Elsevier, 2009).
47. Novoselov, K. S. et al. Electric field effect in atomically thin carbon films. *Science* **306**, 666–669 (2004).
48. Baumgarten, L. & Kierfeld, J. Buckling of thermally fluctuating spherical shells: parameter renormalization and thermally activated barrier crossing. *Phys. Rev. E* **97**, 052801 (2018).
49. Schmidt, C. F. et al. Existence of a flat phase in red cell membrane skeletons. *Science* **259**, 952–955 (1993).
50. Yalonetskaya, A., Mondragon, A. A., Hintze, Z. J., Holmes, S. & McCall, K. Nuclear degradation dynamics in a nonapoptotic programmed cell death. *Cell Death Differ.* **27**, 711–724 (2020).
51. Düring, G., Josserand, C., Krstulovic, G. & Rica, S. Strong turbulence for vibrating plates: emergence of a Kolmogorov spectrum. *Phys. Rev. Fluids* **4**, 064804 (2019).
52. Swift, J. et al. Nuclear lamin-A scales with tissue stiffness and enhances matrix-directed differentiation. *Science* **341**, 1240104 (2013).
53. Schulze, S. R. et al. Molecular genetic analysis of the nested *Drosophila melanogaster* lamin C gene. *Genetics* **171**, 185–196 (2005).
54. Riemer, D. et al. Expression of *Drosophila* lamin C is developmentally regulated: analogies with vertebrate A-type lamins. *J. Cell Sci.* **108**, 3189–3198 (1995).
55. Agrawal, V., Pandey, V. & Mitra, D. Active buckling of pressurized spherical shells: Monte Carlo simulation. Preprint at https://arxiv.org/abs/2206.14172 (2022).

56. Chakrabarti, B. et al. Flexible filaments buckle into helicoidal shapes in strong compressional flows. *Nat. Phys.* **16**, 689–694 (2020).
57. Loubet, B., Seifert, U. & Lomholt, M. A. Effective tension and fluctuations in active membranes. *Phys. Rev. E* **85**, 031913 (2012).
58. Vutukuri, H. R. et al. Active particles induce large shape deformations in giant lipid vesicles. *Nature* **586**, 52–56 (2020).
59. Bausch, A. R. & Kroy, K. A bottom-up approach to cell mechanics. *Nat. Phys.* **2**, 231–238 (2006).
60. Hampoelz, B. et al. Microtubule-induced nuclear envelope fluctuations control chromatin dynamics in *Drosophila* embryos. *Development* **138**, 3377–3386 (2011).
61. Deviri, D. & Safran, S. A. Balance of osmotic pressures determines the nuclear-to-cytoplasmic volume ratio of the cell. *Proc. Natl Acad. Sci. USA* **119**, e2118301119 (2022).
62. Lemiére, J., Real-Calderon, P., Holt, L. J., Fai, T. G. & Chang, F. Control of nuclear size by osmotic forces in *Schizosaccharomyces pombe*. *eLife* **11**, e76075 (2022).
63. Cosgrove, B. D. et al. Nuclear envelope wrinkling predicts mesenchymal progenitor cell mechano-response in 2D and 3D microenvironments. *Biomaterials* **270**, 120662 (2021).
64. Elosegui-Artola, A. et al. Force triggers YAP nuclear entry by regulating transport across nuclear pores. *Cell* **171**, 1397–1410.e14 (2017).
65. Makhija, E., Jokhun, D. S. & Shivashankar, G. V. Nuclear deformability and telomere dynamics are regulated by cell geometric constraints. *Proc. Natl Acad. Sci. USA* **113**, E32–E40 (2016).
66. Kelpsch, D. J., Groen, C. M., Fagan, T. N., Sudhir, S. & Tootle, T. L. Fascin regulates nuclear actin during *Drosophila* oogenesis. *Mol. Biol. Cell* **27**, 2965–2979 (2016).
67. Dialynas, G., Speese, S., Budnik, V., Geyer, P. K. & Wallrath, L. L. The role of *Drosophila* lamin C in muscle function and gene expression. *Development* **137**, 3067–3077 (2010).

Methods

Supplementary Information provides detailed descriptions of the experimental methods, image processing, simulations and theory.

Experiments

A list of fly lines used for this study can be found in Supplementary Table 1. In short, ovaries were removed from well-fed flies and cultured ex vivo[68] for 1–4 h. Images were acquired using laser scanning confocal microscopy with a ×40/1.2-numerical-aperture water or ×63/1.4-numerical-aperture oil objective. For immunofluorescence, ovaries were fixed in 4% (w/v) paraformaldehyde and stained with Alexa Fluor 568 Phalloidin, Hoechst and antibodies against lamin C or trimethylated histone H3K9. Perturbations were performed by adding NaCl-spiked culture medium, water or small-molecule inhibitors to the culture medium under the following final conditions: 1.5× original osmolarity (hypertonic shock), 0.5× osmolarity (hypotonic shock), 9 mg ml^{-1} colchicine or 10 µg ml^{-1} cytochalasin D.

Image processing

NEs were segmented and their coordinates were extracted using Fiji and the MorphoLibJ plug-in[69,70]. Custom-built MATLAB (R2022a) code[71] was used to perform the least-squares fits to determine the spherical harmonic coefficients up to the cutoff mode number $l_{\max} = 25$, which corresponds to an angular scale of roughly 7°, as well as to measure the LamC:Nup107 ratio over the developmental time.

Simulations

We use the pseudo-spectral solver Dedalus 3 (ref. 72) to solve the Langevin equation derived from the non-Euclidean elastic free energy (equation (3)) accounting for hydrodynamic interactions with a viscous environment[15,73] (Supplementary Information provides the details and validations). Due to the stiffness of the equations governing the dynamics of plates and shells, the simulations of such thin surfaces is numerically expensive. We simulate the partial differential equations on a 512 × 256 Driscoll–Healy spherical coordinate grid, for 3×10^5 timesteps using the MIT Supercloud cluster[74]. Each simulation is run on 32 cores for a total of ~360 h of CPU time per simulation. Additional processing to study the simulation results used the pyshtools library[75]. The fact that the power spectrum P_l does not qualitatively change when the nuclear radius R increases suggests that the preferred curvature radius R_c is rather large. In simulations, we, thus, set the preferred curvature radius to $R_c = 20R$ (Supplementary Section IV-4). Consistent with experiments (Fig. 2c), the appearance of a plateau region in the power spectrum P_l at small angular numbers is suppressed for this choice of R_c (Supplementary Section IV-2.1 and Supplementary Fig. 8). Indeed, the typical length scale above which finite-curvature effects become visible is $L_{\mathrm{el}} = R\gamma^{-1/4}\sqrt{R_c/R}$, which is approximately equal to $R/2$ for FvK number $\gamma = 10^4$ and $R_c = 20R$. Supplementary Section IV-4 provides further details on parameter selections.

Reporting summary

Further information on research design is available in the Nature Portfolio Reporting Summary linked to this article.

Data availability

All data supporting the findings of this work are available within the paper and its Supplementary Information. Higher-resolution images, point cloud data, spherical harmonic processing codes and spreadsheets containing the experimental data points shown in the plots are available via Figshare at https://doi.org/10.6084/m9.figshare.23800287. Due to file-size limitations, the raw microscopy data are available from the corresponding authors upon request.

Code availability

The code used for numerical simulations is publicly available via GitHub at https://github.com/NicoRomeo/d3shell.

References

68. Prasad, M. & Montell, D. J. Cellular and molecular mechanisms of border cell migration analyzed using time-lapse live-cell imaging. *Dev. Cell* **12**, 997–1005 (2007).
69. Schindelin, J. et al. Fiji: an open-source platform for biological-image analysis. *Nat. Methods* **9**, 676–682 (2012).
70. Legland, D., Arganda-Carreras, I. & Andrey, P. MorphoLibJ: integrated library and plugins for mathematical morphology with ImageJ. *Bioinformatics* **32**, 3532–3534 (2016).
71. Mietke, A. *Dynamics of Active Surfaces*. PhD thesis, Technische Univ. Dresden (2018).
72. Burns, K. J., Vasil, G. M., Oishi, J. S., Lecoanet, D. & Brown, B. P. Dedalus: a flexible framework for numerical simulations with spectral methods. *Phys. Rev. Research* **2**, 023068 (2020).
73. Lin, L. C.-L. & Brown, F. L. H. Brownian dynamics in Fourier space: membrane simulations over long length and time scales. *Phys. Rev. Lett.* **93**, 256001 (2004).
74. Reuther, A. et al. Interactive supercomputing on 40,000 cores for machine learning and data analysis. In *2018 IEEE High Performance Extreme Computing Conference (HPEC)* 1–6 (IEEE, 2018).
75. Wieczorek, M. A. & Meschede, M. SHTools: tools for working with spherical harmonics. *Geochem. Geophys. Geosyst.* **19**, 2574–2592 (2018).

Acknowledgements

We thank the MIT SuperCloud and Lincoln Laboratory Supercomputing Center for providing high-performance computing resources that have contributed to the research results reported in this paper. We thank M. Kardar, R. D. Kamm, E. Folker, M. A. Collins and D. P. Holmes for helpful discussions. This work was supported by a MathWorks Science Fellowship (N.R.), NSF Award DMS-1952706 (J.D. and N.R.), Sloan Foundation Grant G-2021-16758 (J.D.), MIT Mathematics Robert E. Collins Distinguished Scholar Fund (J.D.), Feodor Lynen Research Fellowship from the Humboldt Foundation (J.F.T.), Jarve Fund MIT grant (A.C.M. and J.D.) and the National Institute of General Medical Sciences of the National Institutes of Health under award no. R01GM144115 (A.C.M). N.R. and J.F.T. acknowledge participation in the KITP online workshop 'The Physics of Elastic Films: from Biological Membranes to Extreme Mechanics' supported in part by the National Science Foundation under grant no. NSF PHY-1748958.

Author contributions

J.I.A., J.A.J., N.R., J.F.T., J.D. and A.C.M. conceived the project. J.I.A. and J.A.J. designed and conducted the experiments. N.R., K.J.B. and J.F.T. designed and implemented the numerical simulations. N.R. and A.M. performed the analytical calculations. J.A.J. and N.R. performed the image and data analyses. N.R., J.A.J., J.I.A. and J.D. wrote the original paper, with input from all authors. All authors revised the paper.

Competing interests

The authors declare no competing interests.

Additional information

Supplementary information The online version contains supplementary material available at https://doi.org/10.1038/s41567-023-02216-y.

Correspondence and requests for materials should be addressed to Jörn Dunkel or Jasmin Imran Alsous.

Peer review information *Nature Physics* thanks Stephanie Höhn and the other, anonymous, reviewer(s) for their contribution to the peer review of this work.

Reprints and permissions information is available at www.nature.com/reprints.

nature portfolio

Corresponding author(s): Jörn Dunkel, Jasmin Imran Alsous

Last updated by author(s): Jul 26, 2023

Reporting Summary

Nature Portfolio wishes to improve the reproducibility of the work that we publish. This form provides structure for consistency and transparency in reporting. For further information on Nature Portfolio policies, see our Editorial Policies and the Editorial Policy Checklist.

Statistics

For all statistical analyses, confirm that the following items are present in the figure legend, table legend, main text, or Methods section.

n/a	Confirmed	
☐	☒	The exact sample size (*n*) for each experimental group/condition, given as a discrete number and unit of measurement
☐	☒	A statement on whether measurements were taken from distinct samples or whether the same sample was measured repeatedly
☐	☒	The statistical test(s) used AND whether they are one- or two-sided *Only common tests should be described solely by name; describe more complex techniques in the Methods section.*
☐	☒	A description of all covariates tested
☐	☒	A description of any assumptions or corrections, such as tests of normality and adjustment for multiple comparisons
☐	☒	A full description of the statistical parameters including central tendency (e.g. means) or other basic estimates (e.g. regression coefficient) AND variation (e.g. standard deviation) or associated estimates of uncertainty (e.g. confidence intervals)
☐	☒	For null hypothesis testing, the test statistic (e.g. F, t, r) with confidence intervals, effect sizes, degrees of freedom and P value noted *Give P values as exact values whenever suitable.*
☒	☐	For Bayesian analysis, information on the choice of priors and Markov chain Monte Carlo settings
☒	☐	For hierarchical and complex designs, identification of the appropriate level for tests and full reporting of outcomes
☒	☐	Estimates of effect sizes (e.g. Cohen's d, Pearson's r), indicating how they were calculated

Our web collection on statistics for biologists contains articles on many of the points above.

Software and code

Policy information about availability of computer code

Data collection	Microscopy: Zeiss Zen Black.
Data analysis	Image analysis: Fiji (with MorphoLibJ plugins). Data analysis: custom MATLAB code. Simulations: custom python code wrapping Dedalus 3 (see github link in manuscript), and custom MATLAB code. Figure making: Adobe Illustrator.

For manuscripts utilizing custom algorithms or software that are central to the research but not yet described in published literature, software must be made available to editors and reviewers. We strongly encourage code deposition in a community repository (e.g. GitHub). See the Nature Portfolio guidelines for submitting code & software for further information.

Data

Policy information about availability of data

All manuscripts must include a data availability statement. This statement should provide the following information, where applicable:

- Accession codes, unique identifiers, or web links for publicly available datasets
- A description of any restrictions on data availability
- For clinical datasets or third party data, please ensure that the statement adheres to our policy

This work used no publicly available datasets. All data generated during this study is available upon request.

Human research participants

Policy information about studies involving human research participants and Sex and Gender in Research.

Reporting on sex and gender	N/A
Population characteristics	N/A
Recruitment	N/A
Ethics oversight	N/A

Note that full information on the approval of the study protocol must also be provided in the manuscript.

Field-specific reporting

Please select the one below that is the best fit for your research. If you are not sure, read the appropriate sections before making your selection.

☒ Life sciences ☐ Behavioural & social sciences ☐ Ecological, evolutionary & environmental sciences

For a reference copy of the document with all sections, see nature.com/documents/nr-reporting-summary-flat.pdf

Life sciences study design

All studies must disclose on these points even when the disclosure is negative.

Sample size	No sample sizes were pre-determined. Sample sizes were deemed sufficient to ensure differences between conditions (e.g. wild type, colchicine addition, osmotic shock) did not result simply from biological variability between samples.
Data exclusions	No data were excluded from the analyses.
Replication	For each condition (e.g. wild type, hypotonic shock, hypertonic shock, drug additions, LamC::GFP intensity), data were collected on multiple days from multiple experiments, each of which included egg chambers from multiple flies.
Randomization	No randomization was necessary, as samples were grouped by genotype or applied perturbation.
Blinding	No blinding was performed, and data analysis processes were identical for all samples.

Reporting for specific materials, systems and methods

We require information from authors about some types of materials, experimental systems and methods used in many studies. Here, indicate whether each material, system or method listed is relevant to your study. If you are not sure if a list item applies to your research, read the appropriate section before selecting a response.

Materials & experimental systems

n/a	Involved in the study	
☐	☒	Antibodies
☒	☐	Eukaryotic cell lines
☒	☐	Palaeontology and archaeology
☐	☒	Animals and other organisms
☒	☐	Clinical data
☒	☐	Dual use research of concern

Methods

n/a	Involved in the study	
☒	☐	ChIP-seq
☒	☐	Flow cytometry
☒	☐	MRI-based neuroimaging

Antibodies

Antibodies used	1. Mouse anti-Lamin C (Developmental Studies Hybridoma Bank LC28.26, concentrate) 2. Rabbit anti-trimethylated H3K9 (Abcam ab8898, gift from the Yamashita lab, Whitehead Institute for Biomedical Research, MIT) 3. Goat anti-mouse Alexa-647 (ThermoFisher Scientific A-21235) 4. Goat anti-rabbit Alexa-488 (ThermoFisher Scientific A-11008)
Validation	1. Mouse anti-Lamin C was used according to recommendations from the supplier. Our immunofluorescence results match the

Validation	localization and intensity decrease with egg chamber age observed using a GFP-tagged version of Lamin C. Additionally, the original study in which the antibody was developed assayed its specificity using western blotting and immunofluorescence (Riemer, Stuurman, et al. Journal of Cell Science 1995). 2. While the rabbit anti-H3K9me3 antibody has not been assessed for use in Drosophila by the manufacturer, it has been used in multiple previous studies by other groups; for one such study in the Drosophila egg chamber, please see Wang et al. PLoS Genetics 2011.

Animals and other research organisms

Policy information about studies involving animals; ARRIVE guidelines recommended for reporting animal research, and Sex and Gender in Research

Laboratory animals	Drosophila melanogaster (fruit fly); 4 to 14 days of age. Strains are detailed in Supplementary Material Table 1.
Wild animals	N/A
Reporting on sex	This study investigated the germline cell cluster giving rise to the egg cell, and as such only involved female flies. Sex is therefore not reported in the study.
Field-collected samples	N/A
Ethics oversight	N/A

Note that full information on the approval of the study protocol must also be provided in the manuscript.